Smoke of extreme Australian bushfires observed in the stratosphere over Punta Arenas, Chile, in January 2020: optical thickness, lidar ratios, and depolarization ratios at 355 and 532 nm

Kevin Ohneiser[1], Albert Ansmann[1], Holger Baars[1], Patric Seifert[1], Boris Barja[2], Cristofer Jimenez[1], Martin Radenz[1], Audrey Teisseire[1], Athina Floutsi[1], Moritz Haarig[1], Andreas Foth[3], Alexandra Chudnovsky[4], Ronny Engelmann[1], Félix Zamorano[2], Johannes Bühl[1], and Ulla Wandinger[1]

[1]Leibniz Institute for Tropospheric Research, Leipzig, Germany
[2]Atmospheric Research Laboratory, University of Magallanes, Punta Arenas, Chile
[3]Leipzig Institute for Meteorology, University of Leipzig, Leipzig, Germany
[4]Tel Aviv University, Porter School of Earth Sciences and Environment, Tel Aviv, Israel

Correspondence: ohneiser@tropos.de

Abstract.

We present particle optical properties of stratospheric smoke layers observed with multiwavelength polarization/Raman lidar over Punta Arenas (53.2°S, 70.9°W), Chile, at the southernmost tip of South America in January 2020. The smoke originated from the record-breaking bushfires in Australia. The stratospheric aerosol optical thickness reached values up to 0.85 at 532 nm in mid January 2020. Main goal of this rapid communication letter is to provide first stratospheric measurements of smoke extinction-to-backscatter ratios (lidar ratios) and particle linear depolarization ratios at 355 and 532 nm wavelength. These aerosol parameters are important input parameters in the analysis of spaceborne CALIPSO and Aeolus lidar observations of the Australian smoke spreading over large parts of the southern hemisphere in January and February 2020 up to heights around 30 km. Lidar and depolarization ratios, simultaneously measured at 355 and 532 nm, are of key importance regarding the homogenization of the overall Aeolus (355 nm wavelength) and CALIPSO (532 nm wavelength) lidar data sets documenting the spread of the smoke and the decay of the stratospheric perturbation which will be observable over the entire year 2020. We found typical values and spectral dependencies of the lidar ratio and linear depolarization ratio for aged stratospheric smoke. At 355 nm, the lidar ratio and depolarization ratio ranged from 53-97 sr (mean of 71 sr) and 0.2-0.26 (mean of 0.23), respectively. At 532 nm, the lidar ratios were higher (75-112 sr, mean of 97 sr) and the depolarization ratios were lower with values of 0.14-0.22 (mean of 0.18). The determined depolarization ratios for aged Australian smoke are in very good agreement with respective ones for aged Canadian smoke, observed with lidar in stratospheric smoke layers over central Europe in the summer of 2017. The much higher 532 nm lidar ratios, however, indicate stronger absorption by the Australian smoke particles.

1 Introduction

Massive bushfires fueled by high, record-breaking temperatures were raging in southeastern Australia in the summer season of 2019-2020 after months of extreme drought (Australian Bureau of Meteorology, 2020). These were the worst wildfires

since decades. The enormous fire activity triggered strong pyrocumulonimbus (pyro-Cb) convection (Fromm and Servranckx, 2003; Fromm et al., 2010) in the last days of December 2019 and in January 2020 as our analysis revealed (Himawari, 2020; Himawari-Kachelmann-Wetter, 2020; MODIS, 2020a). The pyro-Cb towers reached heights of up to 17 km (MODIS, 2020a) and lifted enormous amounts of fire smoke into the upper troposphere and lower stratosphere (UTLS) as will be discussed in

5 Sect. 3. Absorption of sunlight by the black-carbon-containing smoke particles caused warming of the smoke layers and further ascent of the aerosol particles (Boers et al., 2010; de Laat et al., 2012). The prevailing westerly winds transported the smoke layers to South America within 8-14 days. First stratospheric smoke layers of the 2019-2020 Australian burning season were detected with our lidar system over Punta Arenas, Chile, at the southernmost tip of South America in the evening of 5 January 2020, and since then almost continuously until the end of January 2020 (and still in July 2020). The layers over Punta Arenas

10 reached heights of 25-30 km at the end of January caused by diabatic heating of the smoke layers.

Similar to the spread of the Canadian smoke which covered large parts of the lower stratosphere in the northern hemisphere in the summer and autumn of 2017 (Khaykin et al., 2018; Baars et al., 2019b; Hu et al., 2019; Kloss et al., 2019) we expect a strong perturbation of the stratospheric aerosol conditions in the southern hemisphere in 2020. And similar to the northern hemispheric smoke event in 2017, the decay of the perturbation may last longer than 6 months (Baars et al., 2019b; Kloss

15 et al., 2019). These significantly changed stratospheric aerosol conditions have the potential to sensitively influence radiative transfer (Boers et al., 2010; Ditas et al., 2018; Kloss et al., 2019; Yu et al., 2019), heterogeneous ice nucleation in cloud layers (Ullrich et al., 2017), and heterogeneous chemical reactions (Yu et al., 2019) by providing surfaces for, e.g., chlorine activation (McConnell and Jin, 2020). Furthermore, such events enriches the natural soot particle reservoir between 20-30 km (Renard et al., 2008).

20 The spaceborne CALIPSO (Cloud–Aerosol Lidar and Infrared Pathfinder Satellite Observation) lidar (Winker et al., 2009; Omar et al., 2009; Khaykin et al., 2018; Kar et al., 2019) and the Aeolus lidar of the European Space Agency (ESA) (Stoffelen et al., 2005; ESA, 2008; Lux et al., 2020; Witschas et al., 2020; Ansmann et al., 2007; Flamant et al., 2008) will significantly contribute to the monitoring and documentation of the spread of the smoke across the southern hemisphere and of the decay of the stratospheric perturbation in 2020. Passive remote sensing as used by Khaykin et al. (2018); Ansmann et al. (2018); Hu

25 et al. (2019); Kloss et al. (2019) to characterize the record-breaking 2017 smoke event in the northern hemisphere will be used as well.

In this rapid communication letter, we present first measurements of the particle extinction-to-backscatter ratio (lidar ratio) and particle linear depolarization ratio at 355 and 532 nm for aged stratospheric smoke originating from the extreme Australian bush fires. The observations were performed with our multiwavelength polarization/Raman lidar Polly (described in the next

30 section) at Punta Arenas in southern Chile. These lidar and depolarization ratios are required as input parameters in the data analysis and homogenization of the spaceborne CALIPSO and Aeolus lidar measurements which are conducted at different laser wavelengths, namely at 355 nm in the case of the Aelous lidar and 532 nm in the case of the CALIPSO lidar. The 532 nm lidar ratios are, e.g., needed to accurately retrieve height profiles of the smoke light-extinction coefficients and of smoke aerosol optical thickness (AOT) by means of the CALIPSO lidar. On the other hand, 355 nm particle depolarization ratios are

35 required in the retrieval of the total particle backscatter coefficient and the lidar ratio at 355 nm from Aeolus observations. Lidar

ratios and depolarization ratios measured simultaneously at both 355 and 532 nm wavelengths are a prerequisite in efforts to successfully homogenize the overall Aeolus-CALIPSO data set of smoke optical properties later on. Simultaneously measured lidar ratio and depolarisation ratios are also important parameters in aerosol typing efforts (see, e.g., Burton et al., 2012, 2015; Groß et al., 2013; Nicolae et al., 2018; Papagiannopoulos et al., 2018) with lidars from ground and in space, and to improve optical models developed to simulate the smoke optical properties as a function of particle shape and size characteristics and composition (e.g. Kahnert, 2017; Liu and Mishchenko, 2018, 2020; Luo et al., 2019; Gialitaki et al., 2020). Thus, our Punta Arenas lidar observations in January 2020 can be regarded as an important contribution to the global library of aerosol optical properties.

2   Lidar apparatus and data analysis

The lidar observations at Punta Arenas (53.2°S, 70.9°W, 9 m above sea level, a.s.l.), Chile, were conducted in the framework of the long-term DACAPO-PESO (Dynamics, Aerosol, Cloud And Precipitation Observations in the Pristine Environment of the Southern Ocean, https://dacapo.tropos.de) campaign lasting from November 2018 to the end of 2020. The main goal of DACAPO-PESO is the investigation of aerosol-cloud interaction processes at rather pristine, unpolluted marine conditions. The mobile Leipzig Cloudnet supersite LACROS (Leipzig Aerosol and Cloud Remote Observation System, http://lacros.rsd.tropos.de/) (Bühl et al., 2013, 2016) was run continuously at the University of Magallanes (UMAG) at Punta Arenas and covered two summer and winter seasons of aerosol and cloud observations. LACROS is equipped with a multiwavelength polarization/Raman lidar, a wind Doppler lidar, 35 GHz Doppler cloud radar, ceilometer, disdrometer, and microwave radiometer. In addition, an Aerosol Robotic Network (AERONET) sun photometer (Holben et al., 1998) was operated.

The Polly instrument (*PO*rtab*L*le *L*idar s*Y*stem) (Engelmann et al., 2016) is the key instrument of LACROS for aerosol profiling and installed inside a container. This lidar has 13 channels and continuously measures elastically and Raman backscatter signals at the laser wavelengths of 355, 532, and 1064 nm and respective Raman backscattering wavelengths of 387 and 607 nm (nitrogen Raman scattering) and 407 nm (water vapor Raman scattering) (Baars et al., 2016, 2019b). These polarization/Raman lidar observations permit us to determine height profiles of the particle backscatter coefficient at the laser wavelengths of 355, 532 and 1064 nm wavelength, particle extinction coefficients at 355 and 532 nm, the particle linear depolarization ratio at 355 and 532 nm, and of the water-vapor-to-dry-air mixing ratio by using the Raman lidar return signals of water vapor and nitrogen (Engelmann et al., 2016; Hofer et al., 2017; Dai et al., 2018). The linear depolarization ratio is defined as the cross-polarized-to-co-polarized backscatter ratio. "Co" and "cross" denote the planes of polarization parallel and orthogonal to the plane of linear polarization of the transmitted laser pulses, respectively.

Details of the stratospheric Polly data analysis including an uncertainty discussion is given in the recent publication of Baars et al. (2019b) on stratospheric smoke observations in the northern hemisphere. Auxiliary data are required in the lidar data analysis in form of temperature and pressure profiles in order to calculate and correct for Rayleigh backscatter and extinction influences on the measured lidar return signal profiles. As auxiliary meteorological observations we used GDAS1 (Global Data Assimilation System 1) temperature and pressure profiles with 1° horizontal resolution from the National Weather Service's

National Centers for Environmental Prediction (GDAS, 2020). We checked the quality and accuracy of the GDAS1 profiles by comparison with respective temperature and pressure profiles measured with radiosonde at Punta Arenas airport (daily launch at 12 UTC).

Furthermore, the HYSPLIT model (Hybrid Single Particle Lagrangian Integrated Trajectory Model) (HYSPLIT, 2020; Stein et al., 2015; Rolph et al., 2017) based on GDAS1 reanalysis data was used to calculate 13-day backward trajectories. Cloud observations with the Japanese geostationary weather satellite Himawari 8 (Himawari, 2020; Himawari-Kachelmann-Wetter, 2020) and with MODIS (Moderate Resolution Imaging Spectroradiometer) instruments (MODIS, 2020a) were analyzed to identify and characterize pyro-Cb events. CALIPSO lidar data (CALIPSO, 2020) were finally used to support the complex study of the long-range smoke transport across the Pacific Ocean.

3 Observations

3.1 Smoke transport from Australia to southern South America

The year 2019 was Australia's warmest and driest year on record (Australian Bureau of Meteorology, 2020). These extreme conditions favored strong and long-lasting bushfires during the summer months of 2019-2020. Vigorous, deep pyro-Cb convection developed over the fire areas in southeastern Australia and lifted large amounts of smoke into the UTLS height range. We counted pyro-Cb events over southeastern Australia and the adjacent regions over the Pacific Ocean on more than 20 days during the one-month period from 20 December 2019 to 20 January 2020 by analyzing satellite observations (Himawari, 2020; Himawari-Kachelmann-Wetter, 2020; MODIS, 2020a)

Based on a detailed forward and backward trajectory analysis (HYSPLIT, 2020) we distinguished three regimes of smoke transport. These regimes are highlighted in Fig. 1, backward trajectories for case b in Fig. 1 are presented in Fig. 2. The first regime comprises smoke transport in the troposphere. Smoke injected over the source regions at heights below 10 km widely remained in the troposphere (Fig. 1a). Smoke injected into the UTLS regime at heights from about 12 km to about 16-17 km remaining at heights below 19-20 km belong to the second transport regime. These smoke layer experienced fast eastward advection and reached Punta Arenas withing about 10 days. Such a case is shown in Fig. 1b and will be discussed in more detail below. The smoke layers ascended during the transport by efficient diabatic heating as a result of strong absorption of solar radiation by the black-carbon-containing smoke particles and partly entered the stratospheric range above 19-20 km height. Figure 1c shows an example representing this third regime of smoke transport. The smoke-containing air mass (in Fig. 1c) crossed the Pacific Ocean eastward to about 100°W within 6 days according to HYSPLIT forward trajectories starting at 37.1°S, 152°E, i.e., over the western Pacific, close to the coast of southeastern Australia, at heights of 12-17 km between 18-20 January 2020 (not shown). Caused by diabatic heating and lifting, the smoke layers reached heights above 19-20 km after about 6 days and moved forward with rather low speed. The backward trajectories for Punta Arenas with arrival height from 20-28 km on 25-30 January showed many circular movements west and southwest of Punta Arenas. As a consequence, the air masses stayed southwest of and over Punta Arenas for about 5 days according to OMI (Ozone Monitoring Instrument) observations (OMI, 2020) and left the region not before 30 January 2020. This extended smoke plume covered a region of

about 2000 km (east to west) times 1000 km (north to south) and showed many 500 nm AOT pixels between 1-2 as a mean for the period from 20-31 January 2020 (OMI, 2020). The smoke layer in Fig. 1c with very sharp edges at 20.5 km (base) and 26 km height (top) belongs to this extended smoke field. We observed a stratospheric 532 nm AOT of about 0.35 on 29 January 2020. This opportunity was used to learn more about the ascent rate of the smoke. An almost monotonic lifting was recorded.

5 The top height of the smoke layer ascended with a constant rate of 1 km per day from 25 January (layer top at 22 km) to 30 January (layer top at 27 km). This unusual case will be further discussed in Sect. 3.2 based on the final figure of this article.

Figure 2 provides an impression of the air mass transport from the forest fire regions in southeastern Australia to the southern part of South America. The respective smoke observation at Punta Arenas on 10 January 2020 is shown in Fig. 1b. We performed a detailed HYSPLIT trajectory analysis with 5-13-day forward trajectories starting close to the coast of southeast-
10 ern Australia at heights from 12-17 km between 29 December 2019 and 1 January 2020 and 10-13-day backward trajectories arriving at Punta Arenas above the tropopause between 8-11 January 2020 (HYSPLIT, 2020). Based on the trajectory analysis together with the study of pyro-Cb events over southeastern Australia (Himawari, 2020; Himawari-Kachelmann-Wetter, 2020) and corresponding CB top heights and temperatures and thus maximum possible smoke injection heights (MODIS, 2020a), the following synergistic picture on the smoke transport from southeastern Australia to the southern parts of South America
15 between 28 December 2019 and 10 January 2020 was obtained: A period with coherent and intense pyro-Cb developments, triggered by the extreme fires, started on 28 December 2019 (00:00 UTC) and lasted for almost four days. The strongest pyro-Cb clusters occurred from 30 December, 07:00 UTC, to 31 December 2019, 12:00-15:00 UTC. Huge cloud complexes formed with horizontal extents of 150 km×250 km to 350 km×750 km (Himawari, 2020; Himawari-Kachelmann-Wetter, 2020) and the cloud tops partly reached 16-17 km height (MODIS, 2020a). These cloud towers lifted large amounts of smoke into the
20 ULTS region, mostly up to 15-16 km height.

After dissolution of the clouds the released smoke absorbed solar radiation, heated the air, and probably ascended with a rate of about 1-2 km per day during the first three days after injection as long as the stratospheric smoke AOT (at 550 nm) was on the order of 2 and more, as it was the case according to satellite observations over the Pacific east of Australia (MODIS, 2020b; CALIPSO, 2020; Torres et al., 2020b). Torres et al. (2020b) reported 388 nm AOT values of 1 to >5 in a large smoke
25 field east of New Zealand on 2 January 2020. This smoke field was linked to the pyro-Cb activity over southeastern Australia on 30-31 December 2019. This smoke crossed Punta Arenas on 9-10 January 2020. After about three days, the ascent rate may have been much lower at much lower AOTs over the remote Pacific Ocean. We assume a further ascent by around 2 km during the residual 7 days of the travel towards Punta Arenas. This hypothesis of a strong ascent is in good agreement with modeling studies of ascent rates of Australian smoke layers originating from the rather strong Black Saturday fires (occurring
30 on 7 February 2009 in the Melbourne area) by de Laat et al. (2012). A similar ascent of smoke layers by 5-8 km was observed with CALIPSO during the 10-day travel of smoke layers from the western Canadian fire sources to Leipzig, Germany, in mid August 2017 (Torres et al., 2020a). Thus, all in all, the Australian smoke layers probably ascended by 5-7 km within 10 days on the way from southeastern Australia to Punta Arenas. This ascent has to be taken into consideration in the interpretation of our backward trajectory computations which ignore any diabatic heating effect on air motion.

According to the backward trajectories in Fig. 2 the smoke injection heights were at about 16-17 km height over the identified pyro-Cb areas. This finding is in agreement with the discussion by Torres et al. (2020b) about smoke injection heights required to explain the presented satellite-based AOT observations east of New Zealand on 2 January 2020. All backward trajectories that crossed the pyro-Cb areas on 30-31 December 2019 at heights between 14-17 km (colored trajectories) arrived at Punta Arenas between about 11 and 13 km height (the 12.5 km trajectory ensemble is given in Fig. 2). These air masses descended by about 3-5 km on the travel over the 10000 km distance because of the large-scale meteorological conditions. This descent of the smoke layers was then obviously overcompensated by the assumed ascent by 5-7 km so that finally the smoke was observed between 13 and 15 km height and not between 11 and 13 km as the backward trajectories suggested.

We observed another layer on 10 January 2020 (Fig. 1b, 16-18 km height). The respective backward trajectory analysis (not shown) indicates that this smoke layer needed about two days more than the lower smoke layer to reach Punta Arenas. The air masses had thus two more days to absorb solar radiation and thus to ascend to greater heights.

The CALIPSO observations analyzed from 19 December 2019 to 14 January 2020 (CALIPSO, 2020) corroborate our explanation of the smoke transport. A coherent flow of smoke from southeastern Australia to southern South America was found, mainly in the stratosphere including an increase of the smoke layer top height with increasing transport time. More details to the CALIPSO observations and comparison with our ground-based lidar measurements will be presented in a follow-up article focusing on the entire record-breaking stratospheric Australian smoke event in 2020.

It is worth noting that Foth et al. (2019) discuss a similar bush fire case observed with a Polly instrument at the same site of Punta Arenas in March 2010 (Kanitz et al., 2011)). This case was associated with the occurrence of pyro-Cb over western Australia. Similar long-range transport characteristics were found for the smoke in the upper troposphere at about 12 km height to Punta Arenas in March 2010. The study was based on comprehensive atmospheric modeling in combination with CALIPSO lidar observations. The good agreement between the model results and the observations indicate that self-lifting effects were obviously rather weak in this case and could be ignored. Floutsi et al. (2020) summarized recent aerosol observations in the free troposphere over Punta Arenas (November 2018 to December 2019) and also found a smoke plume (at 11 km height), advected from southern Australia to Punta Arenas within 9-10 days in March 2019.

3.2 Lidar observations of smoke optical properties

Figure 3 presents an example of a lidar measurement of stratospheric smoke over Punta Arenas in January 2020. The full set of derivable smoke optical properties is shown. Two-hour mean profiles of the particle backscatter and extinction coefficients and respective extinction-to-backscatter ratios (lidar ratios) as well as of the particle linear depolarization ratios at 355 and 532 nm are given, measured with the polarization/Raman lidar Polly in the early morning of 9 January 2020. Signal smoothing was applied with window lengths of 500-700 m in the case of the backscatter coefficient and depolarization ratio profiles and 2000-2500 m in the case of the extinction coefficient and lidar ratio profiles. The backscatter coefficients were inter-calibrated in a thin cirrus layer between 6-8 km height assuming wavelength-independent cirrus backscattering and are thus very accurate. The results are noisy (especially for 355 nm, affected by strong Rayleigh attenuation) because the Polly lidar is designed and optimized for tropospheric aerosol observations, and not just for monitoring of stratospheric aerosol events as mentioned

already by Baars et al. (2019b). Nevertheless, the layer mean values for the different optical parameters, highlighted as vertical lines in Fig. 3, provide a clear picture of the optical properties and the underlying shape, size, and composition characteristics of the aged stratospheric smoke particles. As typical for aged smoke, the spectral dependency of the backscatter coefficient is strong, whereas the wavelength dependence of the extinction coefficient (for the short wavelength range from 355 to 532 nm) is weak. As a consequence, the lidar ratio is significantly larger at 532 nm compared to 355 nm. The measured depolarization ratios of around 0.2 (355 nm) and 0.15 (532 nm) are also typical for aged smoke for upper tropospheric and stratospheric heights as found by Burton et al. (2015); Haarig et al. (2018); Hu et al. (2019). If the smoke particles would have an ideal spherical shape (consisting of a black carbon core and a thick organic carbon shell) the depolarization ratio would be close to zero (Haarig et al., 2018) as observed for the Canadian smoke at heights in the middle troposphere. Slight deviations from the ideal spherical form in combination with the monomodal, narrow smoke size distribution (accumulation mode shifted to larger particles with mode diameter of 600 to 700 nm, absence of a coarse mode) (Dahlkötter et al., 2014; Haarig et al., 2018) leads to the observed enhanced depolarization values and the distinct wavelength dependence as recently modeled by Gialitaki et al. (2020) and also suggested by other modeling groups (e.g., Yu et al., 2019; Liu and Mishchenko, 2020). According to Yu et al. (2019), smoke particles consist of an insoluble black carbon (BC) core that is surrounded by an almost spherical shell of organic material and other atmospheric substances.

Table 1 summarizes seven analyzed smoke cases observed over Punta Arenas in January 2020. Layer mean values of geometrical and optical properties layers for two pronounced smoke periods lasting from 8–11 January and from 25-30 January are given. During the second period (26-30 January), the analyzed smoke layers were at heights above 19-20 km (Sect. 3.1, smoke transport regime 3). The 387 nm Raman signal profiles were very noisy at heights above 20 km so that a retrieval of 355 nm smoke extinction profiles were no longer possible. Even the cross-polarized 355 nm signals were too noisy for a trustworthy determination of the respective depolarization ratio (28-30 January 2020). To provide at least estimated pairs of 355 and 532 nm lidar ratios even for these cases, we used accompanying Punta Arenas AERONET photometer observations of 380 nm and 500 nm AOTs to calculate the respective extinction wavelength dependence for the short wavelength range, and applied this wavelength dependence to the 532 nm extinction profiles to estimate the respective profiles of the 355 nm smoke extinction coefficient. Afterwards we estimated the 355 nm smoke AOT and layer mean smoke lidar ratios by combining the measured 355 nm layer-mean backscatter coefficients with the estimated 355 nm extinction coefficients. The resulting lidar ratios are given in parentheses in Table 1. This approach is fully reliable when keeping in consideration that the 500 nm AOT (column integrated tropospheric and startospheric extinction coefficient) is typically around 0.03 in this pristine region of the world, and the AOT values, measured in the second half of January 2020, were mainly between 0.2 and 0.35 and thus clearly dominated by the contribution of light extinction by the smoke particles. We applied this combined lidar-photometer method even to the 8-10 January period and found good agreement (not shown here) between the directly determined and estimated 355 nm lidar ratios.

Large lidar ratios of 75-112 sr were observed at 532 nm indicating strongly absorbing BC containing smoke particles. The lidar ratios at 355 nm were systematically lower, partly by more than 30 sr compared to the ones for 532 nm. This is an unambiguous indication for aged smoke. A review on smoke lidar ratios and depolarization ratios in the troposphere and

stratosphere can be found in Haarig et al. (2018). The mean lidar ratios of the seven cases in Table 1 are 71 sr for 355 nm and 97 sr for 532 nm. For the depolarization ratios we obtain mean values of 0.23 (355 nm) and 0.18 (532 nm). Without going into details here, which may be found in Ansmann et al. (2007); Wandinger et al. (2015); Baars et al. (2019a), the Aeolus lidar transmitting circularly polarized laser pulses at 355 nm would have measured an apparent 355 nm lidar ratio a factor of 1.6

5   higher than observed with Polly in this case with a particle depolarization ratio of 0.23 at 355 nm. In the case of the apparent lidar ratio, light-depolarization is ignored in the Aeolus data analysis.

Next, we compared the mean lidar ratios and depolarization ratios of the Australian bushfire smoke event with the ones observed during the record-breaking Canadian smoke season at Leipzig, Germany, in the night of 22-23 August 2017 (see Table 1, last line). This comparison is highlighted in Fig.4. The similarity of the spectral slopes of the lidar and depolarization

10   ratios for stratospheric Canadian and Australian smoke after long-range transport over more than 10000 km in the northern hemisphere (2017) and in the southern hemisphere (2020) is surprising. Very similar depolarization ratio values point to same shape and size characteristics of aged Canadian and Australian smoke in the stratosphere. Even the depolarization ratio at 1064 nm could be measured at the central European lidar station of Leipzig, Germany, in the case of Canadian smoke (Haarig et al., 2018). The strong wavelength dependence of the depolarization ratio from 355 to 1064 nm and the very low 1064 nm

15   depolarization ratio values is a strong hint that coarse mode smoke particles were absent in the stratosphere.

In contrast to the Canadian and Australian smoke depolarization ratios, the lidar ratios are very different. This difference points to a much stronger light absorption by the Australian smoke particles and is probably related to the different burning material. Australian's forests mainly consist of eucalyptus trees, whereas western Canadian tree types are predominantly pine, fir, aspen, and cedar. For completeness, high 532 nm lidar ratios were also observed in the case of wildfire smoke originating

20   from central Africa (Tesche et al., 2011) and from South Africa (Giannakaki et al., 2016). The African lidar ratios for 355 and 532 nm were found to be almost equal (no pronounced wavelength dependence) which, in turn, is an indication that the measured smoke was relatively fresh (of regional origin), and not aged as observed over Punta Arenas.

Figure 5 (together with Table 1) provides a summarizing overview of our stratospheric lidar observations at Punta Arenas in January 2020. The evolution of the stratospheric perturbation over the southernmost tip of South America is shown in

25   terms of 532 nm smoke AOT, respective stratopsheric mean 532 nm extinction coefficient, and the smoke lidar ratios for both wavelengths. The 355 nm lidar ratios in Fig. 5 are exclusively derived by means of the lidar-photometer retrieval method.

As can be seen in Fig. 5a, a two-layer structure developed with a lower layer at heights below about 18 km (Sect. 3.1, smoke transport regime 2) and above 18 km height (smoke transport regime 3). Vertical depths ranged from a few hundreds of meters up to several kilometers, and reached partly values of 6 km. The depolarization ratio observations suggest even different smoke

30   types (or of different age) with slightly different shape properties in the lower and upper layer. The higher depolarization ratios indicating less spherical particle shapes are found in the upper layer.

The ascent of the smoke layer above 20 km is visible between 25 and 30 January. As discussed in Sect. 3.1, this layer observed over Punta Areas was part of a large smoke field (with an extent of 1000 km times 2000 km). According to OMI (2020), the mean 500 nm AOT was around 0.6-0.7 in this smoke field for the 20-31 January period and mean peak values were

35   close to 2. Punta Arenas was always at the rim of the smoke area. The lidar measured the highest stratospheric 532 nm AOTs

of 0.25-0.35 on 28-30 January 2020. As can be seen in Fig. 5a, the top height of the smoke layer steadily moved upward by 1 km per day from 25-30 January 2020. Such a strong ascent rate of 1 km per day was also found by de Laat et al. (2012) for the Black Saturday fire smoke in February 2009, however for AOTs close to 3.5. Ascent rates of about 1 km per day were also derived from CALIPSO observations for the optically dense Canadian smoke layers in the summer 2017 during the first

5   5 days of long-range transport after the injection into the UTLS region on 13 August 2017 (Torres et al., 2020a). It should be mentioned that the backward trajectories arriving at Punta Arenas did not indicate any dynamically induced lifting during the 20-31 Januray 2020 period so that the observed ascent is probably entirely the result of the absorption of solar radiation by the black-carbon-containing smoke particles.

Figure 5b shows that the 532 nm AOT was above the stratospheric background level of 0.002 by 2-4 orders of magnitude

10 in January 2020. Sakai et al. (2016) presents stratospheric aerosol backscatter observations for Lauder, New Zealand, from 1992-2015. By assuming a typical lidar ratio of 50 sr at 532 nm for stratospheric sulfuric acid droplets the minimum column-integrated backscatter coefficients of Lauder correspond to minimum stratospheric AOT values of 0.002 (see dashed line in Fig. 5b).

The highest smoke-related 532 nm AOT value of 0.85 was found in the morning of 17 January 2020. The profile of the

15 smoke backscatter coefficient was multiplied by the 532 nm smoke lidar ratio of 95 sr to obtain an estimate for the 532 nm AOT. For a lidar ratio of 80 sr (also a realistic smoke lidar ratio) the stratospheric AOT would decrease to 0.71, a value close to the maximum 532 nm AOT of 0.6 observed over Leipzig during the noon hours on 22 August 2017 when the densest Canadian smoke plumes crossed Leipzig. The 532 nm AOT remained high with most values from 0.02 to 0.2 in January 2020. Most smoke extinction coefficients were on the order of 10-100 Mm^{-1} in January 2020.

20 Finally, Fig. 5d shows the derived lidar ratios which were high with values mostly between 75-112 sr at 532 nm and much lower for the wavelength of 355 nm. As mentioned, this unique wavelength dependence is a clear signature for aged smoke after long range transport. The opposite is the case, e.g, for urban haze and anthropogenic particles in general. Then the 355 nm lidar ratio is significantly higher than the 532 nm lidar ratio (Müller et al., 2005, 2007).

The ongoing lidar observations at Punta Arenas persently (unitil May 2020) show a very pronounced and geometrically deep

25 smoke layer from about 10 to 20 km height, and frequently thin layers around 25 km height. The AOT values are still clearly enhanced with typical values around 0.05 in March and April 2020. The stratospheric perturbation in the southern hemisphere, triggered by several periods with strong pyro-Cb activity over the southeastern Australian region in December and January 2020, was much stronger than the one in the northern hemisphere in the summer and autumn of 2017, which was related to only one strong pyro-Cb event which occurred on 12-13 August 2017 over western Canada (Peterson et al., 2018; Hu et al.,

30 2019; Torres et al., 2020a).

4   Conclusion and Outlook

Important input parameters, required for a trustworthy CALIPSO and Aeolus lidar data analysis of the stratospheric Australian smoke observations, have been presented. Strong perturbations of the stratospheric aerosol conditions with AOT up to 0.85 at

532 nm were recorded with lidar at Punta Arenas, Chile, in January 2020. The stratospheric smoke depolarization ratios of the Australian fire particles were found to be very similar to the ones observed over Europe in aged Canadian smoke in the summer of 2017. Mean values were 0.23 at 355 nm and 0.18 at 532 nm. However, Australian smoke showed much higher lidar ratios (75-112 sr at 532 nm) compared to the Canadian smoke lidar ratios, which indicates stronger light-absorption. As typical for aged smoke, the smoke lidar ratios at 355 nm were lower by 20-30 sr, partly >30 sr compared to the values at 532 nm.

The Polly observations are ongoing until the end of the DACAPO-PESO campaign in late 2020 and thus will cover the entire bushfire season and most of the decay phase of the stratospheric perturbation in the southern hemisphere. As an outlook, follow-up publications are planned concerning the entire documentation of the unique smoke conditions in the troposphere and stratosphere over southern Chile in 2019 and 2020. This will include the analysis of CALIPSO and Aeolous lidar observations to describe the spread of the smoke in the southern hemisphere. We are working also on a detailed comparison of the record-breaking northern hemispheric smoke event (2017) with this record-breaking stratospheric perturbation in the southern hemispheric.

It is expected that the significantly increased particle concentration in the free troposphere over southern South America sensitively influenced cloud evolution and precipitation formation in this region with usually very low particle concentration of marine origin. Regarding future aerosol-cloud-interaction studies in the framework of the DACAPO-PESO campaign, we plan to distinguish and separate time periods with and without smoke pollution from Australia to evaluate the potential impact of smoke on the occurrence and development of liquid-water, mixed-phase and ice clouds, and to continue in this way with our aerosol and cloud studies we started ten years ago (Kanitz et al., 2011; Foth et al., 2019).

5 Data availability

Polly lidar observations (level 0 data, measured signals) are in the PollyNET data base (PollyNET, 2020). LACROS observations (level 0 data) are stored in the Cloudnet data base (http://lacros.rsd.tropos.de). All the analysis products are available at TROPOS upon request (info@tropos.de). Backward trajectories analysis has been supported by air mass transport computation with the NOAA (National Oceanic and Atmospheric Administration) HYSPLIT (HYbrid Single-Particle Lagrangian Integrated Trajectory) model (HYSPLIT, 2020). CALIPSO observations of smoke profiles and smoke AOT are used (CALIPSO, 2020; FIRMS, 2020)), as well as pyro-Cb cloud clusters satellite observations (Himawari, 2020; Himawari-Kachelmann-Wetter, 2020; MODIS, 2020a). Used fire information is provided by FIRMS (Fire Information for Resource Management System) (FIRMS, 2020).

6 Author contributions

The paper was written by KO and AA. The data analysis was perfomed by KO supported by HB, AA, AF, MH, and UW. All other co-authors are involved in the DACAPO-PESO campaign and took care of all measurements during several 4-week travels.

7 Competing interests

The authors declare that they have no conflict of interest.

8 Financial support

TROPOS is involved in the Calibration/Validation (Cal/Val) activities of the Aeolus space mission in the frame of the German
initiative EVAA (Experimental Validation and Assimilation of Aeolus observations) funded by the German Federal Ministry
for Economic Affairs and Energy (BMWi) under grant no. (FKZ) 50EE1721C. The authors acknowledge also support through
the European Research Infrastructure for the observation of Aerosol, Clouds and Trace Gases ACTRIS under grant agreement
no. 654109 and 739530 from the European Union's Horizon 2020 research and innovation programme. We thank AERONET-
Europe for providing an excellent calibration service. AERONET-Europe is part of the ACTRIS project. The DACAOPO-PESO
observations are partly funded by the German Science Foundation (DFG) project PICNICC with project number 408008112.

Acknowledgements. We thank AERONET for their continuous efforts in providing high-quality measurements and products. Aerosol sources
apportionment analysis has been supported by air mass transport computation with the NOAA (National Oceanic and Atmospheric Admin-
istration) HYSPLIT (HYbrid Single-Particle Lagrangian Integrated Trajectory) model using GDAS meteorological data. We also thank the
Himawari-8, Kachelmann-Wetter, CALIPSO, MODIS, VIIRS, and OMI teams for their well-organized easy-to-use internet platforms. Anal-
yses and visualization tools were made available via the Giovanni online data system, developed and maintained by the NASA GES DISC.
The MODIS and VIIRS information from the fires were provided by LANCE FIRMS operated by NASA/GSFC/EOSDIS.

References

AERONET: Aerosol Robotic Network aerosol data base, available at: http://aeronet.gsfc.nasa.gov/, last access: 20 April, 2020.

Australian Bureau of Meteorology: http://www.bom.gov.au/climate/current/annual/aus/

Ansmann, A., Wandinger, U., Le Rille, O., Lajas, D., and Straume, A.: Particle backscatter and extinction profiling with the spacebornehigh-spectral-resolution Doppler lidar ALADIN: methodology and simulations, Appl. Opt., 46, 6606–6622, https://doi.org/10.1364/AO.46.006606, 2007.

Ansmann, A., Baars, H., Chudnovsky, A., Mattis, I., Veselovskii, I., Haarig, M., Seifert, P., Engelmann, R., and Wandinger, U.: Extreme levels of Canadian wildfire smoke in the stratosphere over central Europe on 21–22 August 2017, Atmos. Chem. Phys., 18, 11831-11845, https://doi.org/10.5194/acp-18-11831-2018, 2018.

Baars, H., Kanitz, T., Engelmann, R., Althausen, D., Heese, B., Komppula, M., Preißler, J., Tesche, M., Ansmann, A., Wandinger, U., Lim, J.-H., Ahn, J. Y., Stachlewska, I. S., Amiridis, V., Marinou, E., Seifert, P., Hofer, J., Skupin, A., Schneider, F., Bohlmann, S., Foth, A., Bley, S., Pfüller, A., Giannakaki, E., Lihavainen, H., Viisanen, Y., Hooda, R. K., Pereira, S. N., Bortoli, D., Wagner, F., Mattis, I., Janicka, L., Markowicz, K. M., Achtert, P., Artaxo, P., Pauliquevis, T., Souza, R. A. F., Sharma, V. P., van Zyl, P. G., Beukes, J. P., Sun, J., Rohwer, E. G., Deng, R., Mamouri, R.-E., and Zamorano, F.: An overview of the first decade of PollyNET: an emerging network of automated Raman-polarization lidars for continuous aerosol profiling, Atmos. Chem. Phys., 16, 5111-5137, doi:10.5194/acp-16-5111-2016, 2016.

Baars, H., Geiß, A., Wandinger, U., Herzog, A., Engelmann, R., Bühl, J., Radenz, M., Seifert, P., Althausen, D., Heese, B., Ansmann, A., Martin, A., Leinweber, R., Lehmann, V., Weissmann, M., Cress, A., Filioglou, M., Komppula, M., and Reitebuch, O.: First results from the German Cal/Val activities for Aeolus, in: Proceedings of the 29th International Laser Radar Conference (ILRC), Hefei, Anhui, China, pp. S1–40–S1–43, 2019a.

Baars, H., Ansmann, A., Ohneiser, K., Haarig, M., Engelmann, R., Althausen, D., Hanssen, I., Gausa, M., Pietruczuk, A., Szkop, A., Stachlewska, I. S., Wang, D., Reichardt, J., Skupin, A., Mattis, I., Trickl, T., Vogelmann, H., Navas-Guzmán, F., Haefele, A., Acheson, K., Ruth, A. A., Tatarov, B., Müller, D., Hu, Q., Podvin, T., Goloub, P., Veselovskii, I., Pietras, C., Haeffelin, M., Fréville, P., Sicard, M., Comerón, A., Fernández García, A. J., Molero Menéndez, F., Córdoba-Jabonero, C., Guerrero-Rascado, J. L., Alados-Arboledas, L., Bortoli, D., Costa, M. J., Dionisi, D., Liberti, G. L., Wang, X., Sannino, A., Papagiannopoulos, N., Boselli, A., Mona, L., D'Amico, G., Romano, S., Perrone, M. R., Belegante, L., Nicolae, D., Grigorov, I., Gialitaki, A., Amiridis, V., Soupiona, O., Papayannis, A., Mamouri, R.-E., Nisantzi, A., Heese, B., Hofer, J., Schechner, Y. Y., Wandinger, U., and Pappalardo, G.: The unprecedented 2017–2018 stratospheric smoke event: decay phase and aerosol properties observed with the EARLINET, Atmos. Chem. Phys., 19, 15183–15198, https://doi.org/10.5194/acp-19-15183-2019, 2019b.

Boers, R., de Laat, A. T., Stein Zweers, D. C., and Dirksen, R. J.: Lifting potential of solar-heated aerosol layers, Geophys. Res. Lett., 37, L24802, doi:10.1029/2010GL045171, 2010.

Bühl, J., Seifert, P., Wandinger, U., Baars, H., Kanitz, T., Schmidt, J., Myagkov, A., Engelmann, R., Skupin, A., Heese, B., Klepel, A., Althausen, D., and Ansmann, A.: LACROS: the Leipzig Aerosol and Cloud Remote Observations System, Proc. SPIE 8890, 889002, https://doi.org/10.1117/12.2030911, 2013.

Bühl, J., Seifert, P., Myagkov, A., and Ansmann, A.: Measuring ice- and liquid-water properties in mixed-phase cloud layers at the Leipzig Cloudnet station, Atmos. Chem. Phys., 16, 10609–10620, https://doi.org/10.5194/acp-16-10609-2016, 2016.

Burton, S. P., Ferrare, R. A., Hostetler, C. A., Hair, J. W., Rogers, R. R., Obland, M. D., Butler, C. F., Cook, A. L., Harper, D. B., and Froyd, K. D.: Aerosol classification using airborne High Spectral Resolution Lidar measurements – methodology and examples, Atmos. Meas. Tech., 5, 73-98, https://doi.org/10.5194/amt-5-73-2012, 2012.

Burton, S. P., Hair, J. W., Kahnert, M., Ferrare, R. A., Hostetler, C. A., Cook, A. L., Harper, D. B., Berkoff, T. A., Seaman, S. T., Collins, J. E., Fenn, M. A., and Rogers, R. R.: Observations of the spectral dependence of linear particle depolarization ratio of aerosols using NASA Langley airborne High Spectral Resolution Lidar, Atmos. Chem. Phys., 15, 13453-13473, doi:10.5194/acp-15-13453-2015, 2015.

CALIPSO: Cloud–Aerosol Lidar and Infrared Pathfinder Satellite Observation Lidar Level 2 Vertical Feature Mask data, ValStage1 V3-40, available at https://search.earthdata.nasa.gov/search/granules?p=C1356785518-LARC$\_{\_}$\$ASDC&tl=1567329628!4!!, via the CALIPSO webpage, and https://www-calipso.larc.nasa.gov/products/lidar/browse_images/std_v4_index.php, last access: 20 April, 2020.

Dahlkötter, F., Gysel, M., Sauer, D., Minikin, A., Baumann, R., Seifert, P., Ansmann, A., Fromm, M., Voigt, C., and Weinzierl, B.: The Pagami Creek smoke plume after long-range transport to the upper troposphere over Europe – aerosol properties and black carbon mixing state, Atmos. Chem. Phys., 14, 6111–6137, https://doi.org/10.5194/acp-14-6111-2014, 2014.

Dai, G., Althausen, D., Hofer, J., Engelmann, R., Seifert, P., Bühl, J., Mamouri, R.-E., Wu, S., and Ansmann, A.: Calibration of Raman lidar water vapor profiles by means of AERONET photometer observations and GDAS meteorological data, Atmos. Meas. Tech., 11, 2735–2748, https://doi.org/10.5194/amt-11-2735-2018, 2018.

de Laat, A. T. J., Stein Zweers, D. C., Boers, R., and Tuinder, O. N. E.: A solar escalator: Observational evidence of the self-lifting of smoke and aerosols by absorption of solar radiation in the February 2009 Australian Black Saturday plume, J. Geophys. Res., 117, D04204, doi:10.1029/2011JD017016, 2012.

Ditas, J., Ma, N., Zhang, Y., Assmann, D., Neumaier, M., Riede, H., Karu, E., Williams, J., Scharffe, D., Wang, Q., Saturno, J., Schwarz, J. P., Katich, J. M., McMeeking, G. R., Zahn, A., Hermann, M., Brenninkmeijer, C. A. M., Andreae, M. O., Pöschl, U., Su, H., and Cheng, Y.: Strong impact of wildfires on the abundance and aging of black carbon in the lowermost stratosphere, Proceedings of the National Academy of Sciences, 115, E11595-E11603, doi: 10.1073/pnas.1806868115, 2018.

Engelmann, R., Kanitz, T., Baars, H., Heese, B., Althausen, D., Skupin, A., Wandinger, U., Komppula, M., Stachlewska, I. S., Amiridis, V., Marinou, E., Mattis, I., Linné, H., and Ansmann, A.: The automated multiwavelength Raman polarization and water-vapor lidar PollyXT: the neXT generation, Atmos. Meas. Tech., 9, 1767-1784, doi:10.5194/amt-9-1767-2016, 2016.

ESA: European Space Agency, ADM-Aeolus Science Report, ESA SP-1311, available at: http://esamultimedia.esa.int/docs/730SP-1311_ADM-Aeolusa_FINA_low-res.pdf , 2008.

FIRMS: Fire Information for Resource Management System providing near real-time active fire data from MODIS (Moderate Resolution Imaging Spectroradiometer) and VIIRS (Visible Infrared Imaging Radiometer Suite), fire information available at: https://firms.modaps.eosdis.nasa.gov/active_fire/#firms-shapefile and https://firms.modaps.eosdis.nasa.gov/map/#z:5;c:144.3,-27.9;t:adv-points;d:2019-12-20..2020-01-20;l:firms_viirs, last access: 20 April, 2020.

Flamant, P., Cuesta, J., Denneulin, M. L., Dabas, A., and Huber, D.: ADM-Aeolus retrieval algorithms for aerosol and cloud products, Tellus A, 60, 273–288, doi:10.1111/j.1600-0870.2007.00287.x, 2008.

Floutsi, A. A., Baars, H., Radenz, M., Haarig, M., Yin, Z., Seifert, P., Jimenez, C., Wandinger, U., Engelmann, R., Barja, B., Zamorano, F., and Ansmann, A.: Biomass burning aerosols in the southern hemispheric midlatitudes as observed with a multiwavelength polarization Raman lidar, Atmos. Chem. Phys. Discuss., https://doi.org/10.5194/acp-2020-453, in review, 2020.

Foth, A., Kanitz, T., Engelmann, R., Baars, H., Radenz, M., Seifert, P., Barja, B., Fromm, M., Kalesse, H., and Ansmann, A.: Vertical aerosol distribution in the southern hemispheric midlatitudes as observed with lidar in Punta Arenas, Chile (53.2° S and 70.9° W), during ALPACA, Atmos. Chem. Phys., 19, 6217-6233, https://doi.org/10.5194/acp-19-6217-2019, 2019.

Fromm, M. D., and Servranckx, R.: Transport of forest fire smoke above the tropopause by supercell convection, Geophys. Res. Lett., 30, 1542, doi:10.1029/2002GL016820, 2003.

Fromm, M., Shettle, E. P., Fricke, K. H., Ritter, C., Trickl, T., Giehl, H., Gerding, M., Barnes, J. E., O'Neill, M., Massie, S. T., Blum, U., McDermid, I. S., Leblanc, T., and Deshler, T.: Stratospheric impact of the Chisholm pyrocumulonimbus eruption: 2. Vertical profile perspective, J. Geophys. Res., 113, D08203, doi:10.1029/2007JD009147, 2008.

Fromm, M., Lindsey, D. T., Servranckx, R., Yue, G., Trickl, T., Sica, R., Doucet, P., and Godin-Beekmann, S. E.: The untold story of pyrocumulonimbus, B. Am. Meteorol. Soc., 91, 1193–1209, doi:10.1175/2010bams3004.1, 2010.

GDAS: Global Data Assimilation System, meteorological data base, available at: https://www.ready.noaa.gov/gdas1.php, last access: 20 January, 2020.

Gialitaki, A., Tsekeri, A., Amiridis, V., Ceolato, R., Paulien, L., Kampouri, A., Gkikas, A., Solomos, S., Marinou, E., Haarig, M., Baars, H., Ansmann, A., Lapyonok, T., Lopatin, A., Dubovik, O., Groß, S., Wirth, M., and Balis, D.: Is the near-spherical shape the "new black" for smoke?, Atmos. Chem. Phys. Discuss., https://doi.org/10.5194/acp-2020-22, in review, 2020.

Giannakaki, E., van Zyl, P. G., Müller, D., Balis, D., and Komppula, M.: Optical and microphysical characterization of aerosol layers over South Africa by means of multi-wavelength depolarization and Raman lidar measurements, Atmos. Chem. Phys., 16, 8109–8123, https://doi.org/10.5194/acp-16-8109-2016, 2016.

Groß, S., Esselborn, M., Weinzierl, B., Wirth, M., Fix, A., and Petzold, A.: Aerosol classification by airborne high spectral resolution lidar observations, Atmos. Chem. Phys., 13, 2487-2505, doi:10.5194/acp-13-2487-2013, 2013.

Haarig, M., Ansmann, A., Baars, H., Jimenez, C., Veselovskii, I., Engelmann, R., and Althausen, D.: Depolarization and lidar ratios at 355, 532, and 1064 nm and microphysical properties of aged tropospheric and stratospheric Canadian wildfire smoke, Atmos. Chem. Phys., 18, 11847-11861, https://doi.org/10.5194/acp-18-11847-2018, 2018.

Himawari: Data base of the 8th of the Himawari geostationary weather satellites operated by the Japan Meteorological Agency, cloud information available at: https://himawari8.nict.go.jp/, last access: 20 April, 2020.

Himawari, Kachelmannwetter: Cloud top temperatures based on Himawari-8 cloud observations, available at https://kachelmannwetter.com/de/sat/newsouthwales/top-alarm-10min/20200123-1150z.html, last access: 20 April 2020.

Hofer, J., Althausen, D., Abdullaev, S. F., Makhmudov, A. N., Nazarov, B. I., Schettler, G., Engelmann, R., Baars, H., Fomba, K. W., Müller, K., Heinold, B., Kandler, K., and Ansmann, A.: Long-term profiling of mineral dust and pollution aerosol with multiwave-length polarization Raman lidar at the Central Asian site of Dushanbe, Tajikistan: case studies, Atmos. Chem. Phys., 17, 14559–14577, https://doi.org/10.5194/acp-17-14559-2017, 2017.

Holben, B. N., Eck, T. F., Slutsker, I., Tanré, D., Buis, J. P., Setzer, A., Vermote, E., Reagan, J. A., Kaufman, Y. J., Nakajima, T., Lavenu, F., Jankowiak, I., and Smirnov, A.: AERONET – a federated instrument network and data archive for aerosol characterization, Remote Sens. Environ., 66, 1–16, 1998.

Hu, Q., Goloub, P., Veselovskii, I., Bravo-Aranda, J.-A., Popovici, I. E., Podvin, T., Haeffelin, M., Lopatin, A., Dubovik, O., Pietras, C., Huang, X., Torres, B., and Chen, C.: Long-range-transported Canadian smoke plumes in the lower stratosphere over northern France, Atmos. Chem. Phys., 19, 1173-1193, https://doi.org/10.5194/acp-19-1173-2019, 2019.

HYSPLIT: HYbrid Single-Particle Lagrangian Integrated Trajectory model, backward trajectory calculation tool, available at: http://ready.arl.noaa.gov/HYSPLIT_traj.php, last access: 20 January, 2020.

Kahnert, M.: Optical properties of black carbon aerosols encapsulated in a shell of sulfate: comparison of the closed cell modell with a coated aggregate model, Opt. Express, 25, doi:10.1364/OE.25.024579, 2017.

5   Kanitz, T., Seifert, P., Ansmann, A., Engelmann, R., Althausen, D., Casiccia, C., and Rohwer, E. G.: Contrasting the impact of aerosols at northern and southern midlatitudes on heterogeneous ice formation, Geophys. Res. Lett., 38, L17802, doi:10.1029/2011GL048532, 2011.

Kar, J., Lee, K.-P., Vaughan, M. A., Tackett, J. L., Trepte, C. R., Winker, D. M., Lucker, P. L., and Getzewich, B. J.: CALIPSO level 3 stratospheric aerosol profile product: version 1.00 algorithm description and initial assessment, Atmos. Meas. Tech., 12, 6173–6191, https://doi.org/10.5194/amt-12-6173-2019, 2019.

10   Khaykin, S. M., Godin-Beekmann, S., Hauchecorne, A., Pelon, J., Ravetta, F., and Keckut, P.: Stratospheric smoke with unprecedentedly high backscatter observed by lidars above southern France, Geophys. Res. Lett., 45, https://doi.org/10.1002/2017GL076763, 2018.

Kloss, C., Berthet, G., Sellitto, P., Ploeger, F., Bucci, S., Khaykin, S., Jègou, F., Taha, G., Thomason, L. W., Barret, B., Le Flochmoen, E., von Hobe, M., Bossolasco, A., Bègue, N., and Legras, B.: Transport of the 2017 Canadian wildfire plume to the tropics via the Asian monsoon circulation, Atmos. Chem. Phys., 19, 13547–13567, https://doi.org/10.5194/acp-19-13547-2019, 2019.

15   Liu, L., and Mishchenko, M. I.: Scattering and radiative properties of morphologically complex carbonaceous aerosols: A systematic modeling study. Remote Sens., 10, https://doi:10.3390/rs10101634, 2018.

Liu, L., and Mishchenko, M. I.: Spectrally dependent linear depolarization and lidar ratios for nonspherical smoke aerosols, J. Quant. Spec. Radiat. Trans., 248, https://doi.org/10.1016/j.jqsrt.2020.106953, 2020.

Luo, J., Zhang, Q., Luo, J., Liu, J., Huo, Y., and Zhang, Y.: Optical modeling of black carbon with different coating materials: The effect of
20   coating configurations. J. Geophys. Res. - Atmospheres, 124, 13230– 13253. https://doi.org/10.1029/2019JD031701, 2019.

Lux, O., Lemmerz, C., Weiler, F., Marksteiner, U., Witschas, B., Rahm, S., Geiß, A., and Reitebuch, O.: Intercomparison of wind observations from the European Space Agency's Aeolus satellite mission and the ALADIN Airborne Demonstrator, Atmos. Meas. Tech., 13, 2075–2097, https://doi.org/10.5194/amt-13-2075-2020, 2020.

McConnell, J. C., and Jin, J. J.: Stratospheric ozone chemistry, Atmosphere-Ocean, 46:1, 69–92, https://doi.org/10.3137/ao.460104, 2008.

25   MODIS: Moderate Resolution Imaging Spectroradiometer cloud top height information, available at: https://go.nasa.gov/2YdOaYH, last access: 20 April, 2020a.

MODIS: MODIS aerosol optical depth information, Combined Dark Target, Deep Blue AOT at 550 nm available at: https://worldview.earthdata.nasa.gov/?v=91.53604354847852,-60.483141476646644,204.03604354847852,-5.217516476646644&t=2019-12-31-T07%3A49%3A16Z&l=MODIS_Aqua_Aerosol,Coastlines,Reference_Labels,Reference_Features,VIIRS_SNPP_CorrectedReflectance_
30   TrueColor(hidden),MODIS_Aqua_CorrectedReflectance_TrueColor(hidden),MODIS_Terra_CorrectedReflectance_TrueColor(hidden), last access: 20 April, 2020b.

Müller, D., Mattis, I., Wandinger, U., Ansmann, A., Althausen, A., and Stohl, A.: Raman lidar observations of aged Siberian and Canadian forest fire smoke in the free troposphere over Germany in 2003: Microphysical particle characterization, J. Geophys. Res., 110, D17201, doi:10.1029/2004JD005756, 2005.

35   Müller, D., Ansmann, A., Mattis, I., Tesche, M., Wandinger, U., Althausen, D., and Pisani, G.: Aerosol-type-dependent lidar ratios observed with Raman lidar, J. Geophys. Res., 112, D16202, doi:10.1029/2006JD008292, 2007.

Nicolae, D., Vasilescu, J., Talianu, C., Binietoglou, I., Nicolae, V., Andrei, S., and Antonescu, B.: A neural network aerosol-typing algorithmbased on lidar data, Atmos. Chem. Phys., 18, 14 511–14 537, https://doi.org/10.5194/acp-18-14511-2018, 2018.

Omar, A. H., Winker, D. M., Vaughan, M. A., Hu, Y., Trepte, C. R., Ferrare, R. A., Lee, K. P., Hostetler, C. A., Kittaka, C., Rogers, R. R., and Kuehn, R. E.: The CALIPSO Automated Aerosol Classification and Lidar Ratio Selection Algorithm, J. Atmos. Ocean. Tech., 26, 1994-2014, https://doi.org/10.1175/2009JTECHA1231.1, 2009.

OMI: Ozone Monitoring Instrument data base, time-averaged daily maps of AOT at 500 nm with 1 degree resolution (OMI OMAERUVd v003) from the NASA Earth Observing System (EOS) Aura satellite for January 20-31, 2020, downloaded from Giovanni online data system, maintained by NASA GES DISC. The average AOT was calculated online and downloaded as one GeoTIFF file to ArvGIS environment for further processing and creating maps, AOT data available at: https://earthdata.nasa.gov/earth-observation-data/near-real-time/download-nrt-data/omi-nrt, last access: 20 April 2020.

Papagiannopoulos, N., Mona, L., Amodeo, A., D'Amico, G., Gumà Claramunt, P., Pappalardo, G., Alados-Arboledas, L., Guerrero-Rascado,J. L., Amiridis, V., Kokkalis, P., Apituley, A., Baars, H., Schwarz, A., Wandinger, U., Binietoglou, I., Nicolae, D., Bortoli, D., Comerón,A., Rodríguez-Gómez, A., Sicard, M., Papayannis, A., and Wiegner, M.: An automatic observation-based aerosol typing method forEARLINET, Atmos. Chem. Phys., 18, 15 879–15 901, https://doi.org/10.5194/acp-18-15879-2018, 2018

Peterson, D.A., Campbell, J.R., Hyer, E.J., Fromm, M. D., Kablick III, G. P., Cossuth, J. H., and DeLand, M. T.: Wildfire-driven thunderstorms cause a volcano-like stratospheric injection of smoke. npj Clim Atmos Sci 1, 30, https://doi.org/10.1038/s41612-018-0039-3, 2018.

PollyNet: PollyNET lidar data base, available at: http://polly.rsd.tropos.de/, last access: 8 April 2020

Renard, J.-B., Brogniez, C., Berthet, G., Bourgeois, Q., Gaubicher, B., Chartier, M., Balois, J.-Y., Verwaerde, C., Auriol, F., Francois, P., Daugeron, D., and Engrand, C.: Vertical distribution of the different types of aerosols in the stratosphere: Detection of solid particles and analysis of their spatial variability, J. Geophys. Res., 113, D21303, doi:10.1029/2008JD010150, 2008.

Rolph, G., Stein, A., and Stunder, B.: Real-time Environmental Applications and Display sYstem: READY. Environmental Modelling & Software, 95, 210-228, https://doi.org/10.1016/j.envsoft.2017.06.025, 2017.

Sakai, T., Uchino, O., Nagai, T., Liley, B., Morino, I., and Fujimoto, T.: Long-term variation of stratospheric aerosols observed with lidars over Tsukuba, Japan, from 1982 and Lauder, New Zealand, from 1992 to 2015, J. Geophys. Res. Atmos., 121, 10283-10293, doi:10.1002/2016JD025132, 2016.

Siddaway, J. M., and Petelina, S. V.: Transport and evolution of the 2009 Australian Black Saturday bushfire smoke in the lower stratosphere observed by OSIRIS on Odin, J. Geophys. Res., 116, D06203, doi: 10.1029/2010JD015162, 2011.

Stein, A.F., Draxler, R.R, Rolph, G.D., Stunder, B.J.B., Cohen, M.D., and Ngan, F.: NOAA's HYSPLIT atmospheric transport and dispersion modeling system, Bull. Amer. Meteor. Soc., 96, 2059-2077, http://dx.doi.org/10.1175/BAMS-D-14-00110.1, 2015

Stoffelen, A., Pailleux, J., Källén, E., Vaughan, J. M., Isaksen, L., Flamant, P., Wergen, W., Andersson, E., Schyberg, H., Culoma, A., Meynart, R., Endemann, M., and Ingmann, P.: The atmospheric dynamics mission for global wind field measurement, Bulletin of the American Meteorological Society, 86, 73–88, https://doi.org/10.1175/BAMS-86-1-73, 2005.

Tesche, M., Müller, D., Groß, S., Ansmann, A., Althausen, D., Freudenthaler, V., Weinzierl, B., Veira, A., and Petzold, A.: Optical and microphysical properties of smoke over Cape Verde inferred from multiwavelength lidar measurements. Tellus B, 63, 677–694. doi:10.1111/j.1600-0889.2011.00549.x, 2011.

Torres, O., Bhartia, P. K., Taha, G., Jethva, H., Das, S., Colarco, P., Krotkov, N., Omar, A., and Ahn, C.: Stratospheric Injection of Massive Smoke Plume from Canadian Boreal Fires in 2017 as seen by DSCOVR-EPIC, CALIOP and OMPS-LP Observations. Journal of Geophysical Research: Atmospheres, 125, e2020JD032579, https://doi.org/10.1029/2020JD032579, 2020a.

Torres, O., Jethva, H., Ahn, C., Jaross, G., and Loyola, D. G.: TROPOMI Aerosol Products: Evaluation and Observations of Synoptic Scale Carbonaceous Aerosol Plumes during 2018–2020, Atmos. Meas. Tech. Discuss., https://doi.org/10.5194/amt-2020-124, in review, 2020b.

Ullrich, R., Hoose, C., Möhler, O., Niemand, M., Wagner, R., Höhler, K., Hiranuma, N., Saathoff, H., and Leisner, T.: A new ice nucleation active site parameterization for desert dust and soot, J. Atmos. Sci., 74, 699–717, 2017.

5   Wandinger, U., Amiridis, V., Freudenthaler, V., Komppula, M., Kokkalis, P., Engelmann, R., Marinou, E., and Tsekeri, A.: Validation of ADM-Aeolus L2 aerosol and cloud products employing advanced ground-based lidar measurements (VADAM), in: ADM-Aeolus Science and CAL/VAL Workshop, ESA-ESRIN, Frascati, Italy, ESA-ESRIN, 2015.

Winker, D. M., Vaughan, M. A., Omar, A., Hu, Y., Powell, K. A., Liu, Z., Hunt, W. H., and Young, S. A.: Overview of the CALIPSO mission and CALIOP data processing algorithms, J. Atmos. Oceanic. Techn., 26, 2310-2323, doi:10.1175/2009JTECHA1281.1, 2009.

10   Witschas, B., Lemmerz, C., Geiß, A., Lux, O., Marksteiner, U., Rahm, S., Reitebuch, O., and Weiler, F.: First validation of Aeolus wind observations by airborne Doppler wind lidar measurements, Atmos. Meas. Tech., 13, 2381–2396, https://doi.org/10.5194/amt-13-2381-2020, 2020.

Yu, P., Toon, O. B., Bardeen, C. G., Zhu, Y., Rosenlof, K. H., Portmann, R. W., Thornberry, T. D., Gao, R.-S., Davis, S. M., Wolf, E. T., de Gouw, J., Peterson, D. A., Fromm, M. D., and Robock, A.: Black carbon lofts wildfire smoke high into the stratosphere to form a persistent

15   plume, Science, 365, 587–590, doi: 10.1126/science.aax1748, 2019.

Table 1. Smoke layer mean values of lidar ratios (LR) and depolarization ratios (DR) simultaneously measured at 355 and 532 nm on three subsequent days in January 2020. Tropopause heights (TPH), layer base heights (LBH), geometrical depths (LGD), and AOTs of the stratospheric smoke layers are given in addition. Wavelength (in nm) is indicated in parentheses. The uncertainty in the layer mean values is mainly caused by signal noise estimated to be about 10% (DR, 532 nm), 20% (LR, 532 nm, DR, 355 nm), and 30% (LR, 355 nm). For comparison, values for aged Candian smoke measured over Leipzig, Germany, in August 2017 are given in the last line (Haarig et al., 2018) AERONET photometer observation of AOT wavelength dependence for the short wavelength spectral range (380-500 nm) is used to estimate 355 nm smoke AOT, extinction coefficient, and lidar ratio from the lidar measurements at 532 nm. These value are also given in parentheses (26-30 January 2020).

Date	TPH [km]	LBH [km]	LGD [km]	AOT(355)	AOT(532)	LR(355) [sr]	LR(532) [sr]	DR(355)	DR(532)
8 Jan 2020, 04:30-06:30 UTC	8.8	13.0	1.6	0.07	0.05	83	102	0.23	0.14
9 Jan 2020, 03:56-05:40 UTC	8.9	12.8	2.9	0.19	0.15	53	76	0.20	0.14
10 Jan 2020, 02:25-04:20 UTC	10.2	16.3	2.7	0.21	0.14	97	104	0.26	0.15
26 Jan 2020, 04:27-06:19 UTC	9.8	19.3	3.6	(0.28)	0.16	(75)	112	0.22	0.20
28 Jan 2020, 05:15-07:29 UTC	8.7	20.6	4.4	(0.49)	0.33	(56)	75	–	0.19
29 Jan 2020, 01:45-04:14 UTC	10.8	20.5	5.7	(0.53)	0.31	(70)	106	–	0.21
30 Jan 2020, 02:05-04:30 UTC	11.8	22.0	5.1	(0.45)	0.26	(66)	103	–	0.22
22 Aug 2017, 20:45-00:30 UTC	11.0	15.0	1.0	0.20	0.23	40	66	0.22	0.18
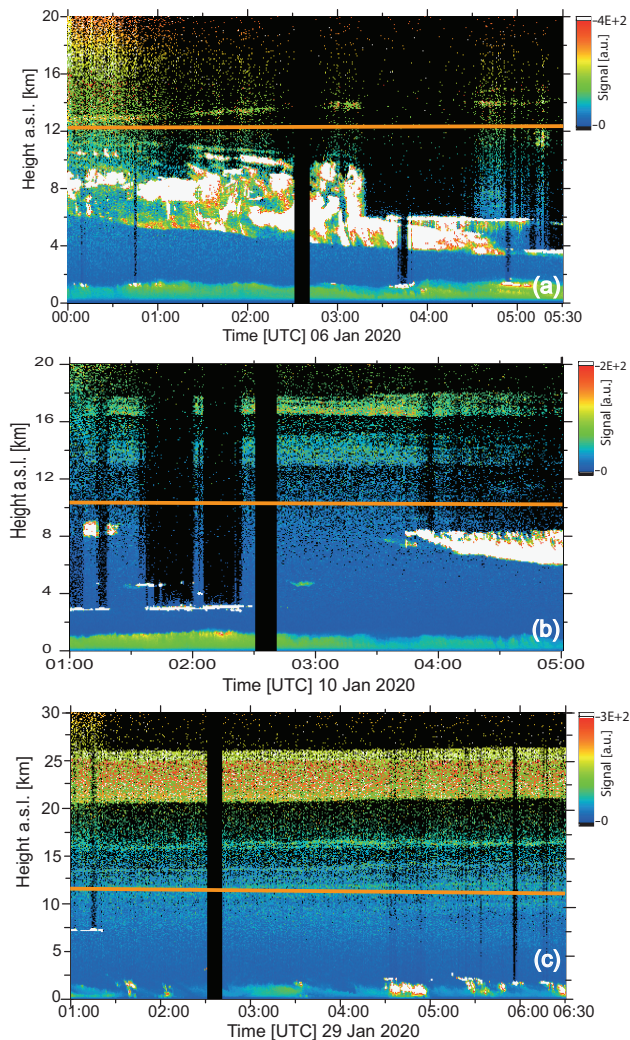
Figure 1. Australian bushfire smoke in the troposphere (a), here the smoke layer extends from 6–11 km at 00:00 UTC and slowly descended with time), and in the stratosphere (a: thin layer at 12.5 km in the beginning and at 14 km at the end, b: two layers from 13-15 km and from 16-18 km height, c: thin layers at 13 and 16 km, and a dense layer from 20-26 km height). The smoke was observed with the lidar at Punta Arenas, Chile, 10000 km downwind of the Australian fire areas on (a) 6 January, (b) 10 January, and (c) 29 January 2020. The range-corrected 1064 nm signal is shown. The tropopause heights according to the Punta Arenas radiosonde (launched at 12:00 UTC, 08:00 local time) are given as orange horizontal lines. Black, column-like filaments above cloud layers (shown as white areas) indicate strong laser pulse attenuation. The large, well-defined black columns (from surface to 20 km) indicate periods of automated depolarization calibration. The complex white areas in (a) above 4 km height indicate ice and mixed-phase clouds which caused ice virga formation (red and yellow). The clouds developed in smoke-containing air (green to blue with a few long-lasting coherent shallow smoke layers in yellow below and above the tropopause). These rather complex cloud features may be related to the occurrence of enhanced levels of smoke INPs (ice-nucleating particles) in the usually very pristine free troposphere with a low amount of very inefficient marine INPs (Kanitz et al., 2011).
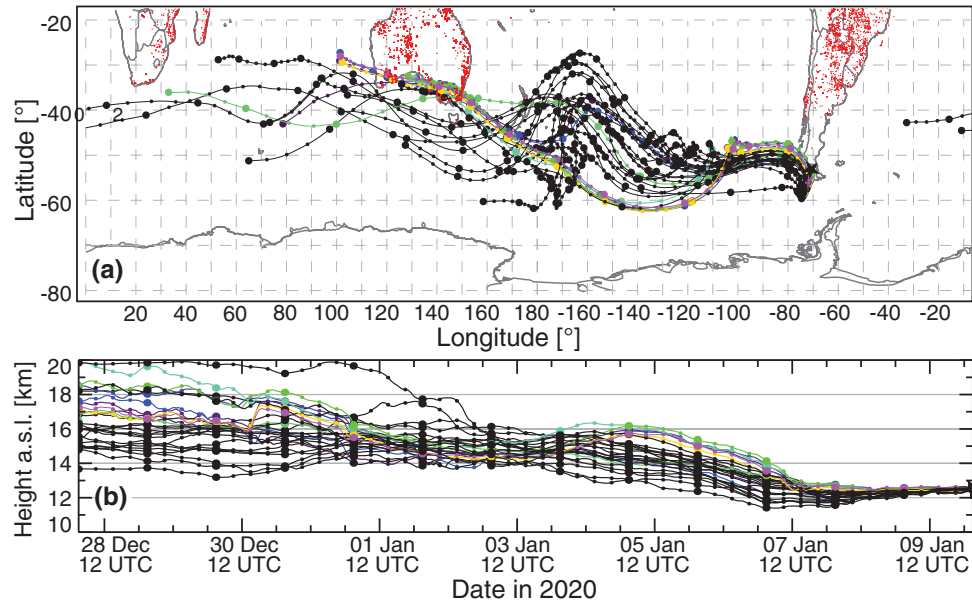
Figure 2. 13-day backward trajectories (HYSPLIT, 2020) arriving at Punta Arenas (black star) on 10 January 2020, 03:00 UTC at 12.5 km height a.s.l. The colored backward trajectories crossed the bushfire and pryroCB areas in southeastern Australia and downwind over the adjacent Pacific Ocean on 30-31 December 2020. Fires occurring between 21 and 30 December 2019 are given as red dots (in a) and provided by FIRMS (2020).
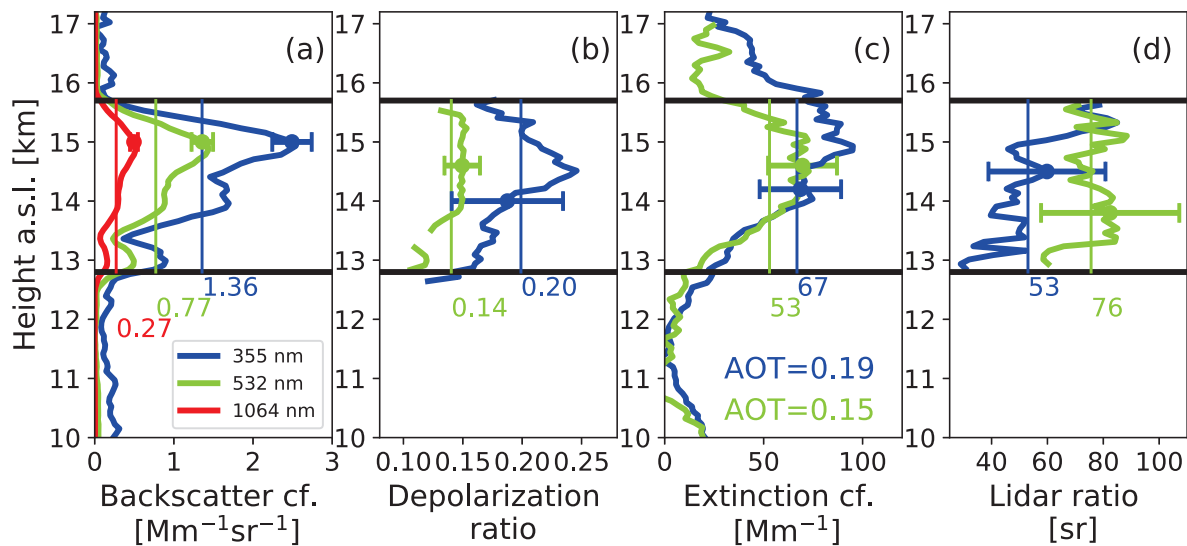
Figure 3. Profiles of smoke optical properties measured with the Polly lidar in the stratosphere over Punta Arenas on 9 January 2020, 03:56-05:40 UTC. Base and top heights of the smoke layer are indicated by black horizontal lines. (a) Particle backscatter coefficient at three wavelengths, (b) particle linear depolarization ratio, (c) smoke extinction coefficient and AOT, and d) smoke extinction-to-backscatter ratio (lidar ratio). Colored vertical lines from layer base to top indicate layer mean values (given also as numbers). Error bars show the estimated uncertainties. In (c) and (d) Raman signal smoothing with window lengths of 2000-2500 m was necessary so that the values around 14-15 km height represent best the extinction coefficients and lidar ratios of the 3 km deep smoke layer.
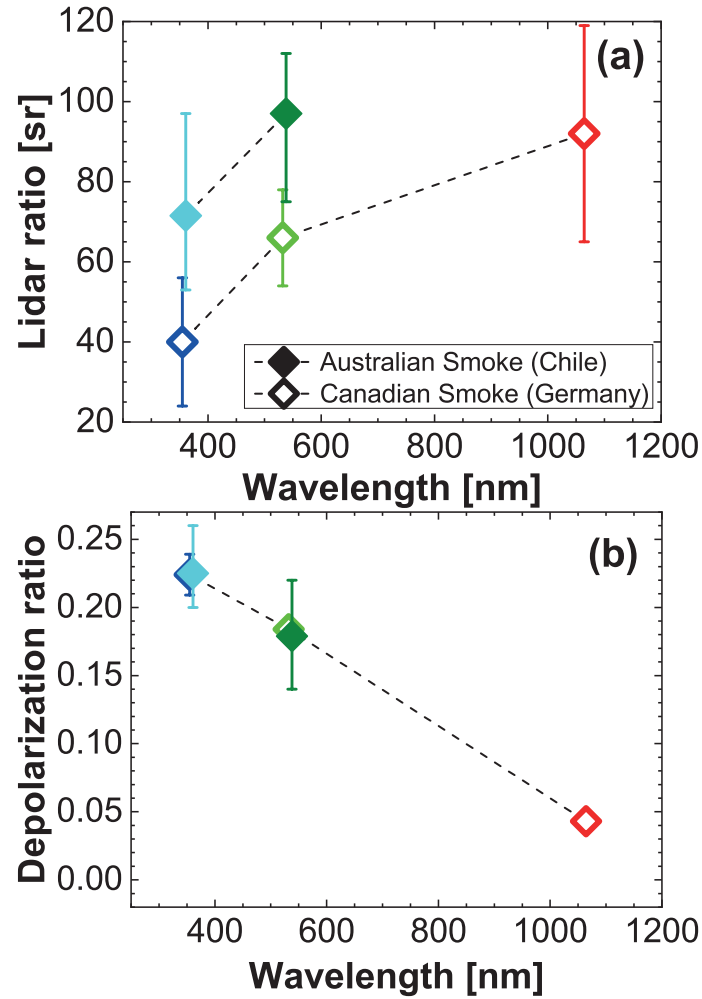
Figure 4. Comparison of the spectral dependence of (a) the lidar ratio and (b) the particle linear depolarization ratio of aged Canadian and Australian smoke as measured in the stratosphere over Leipzig, Germany, on 22 August 2017 (open symbols) and over Punta Arenas, Chile, in January 2020 (closed symbols). In the case of the Australian smoke, mean values of the seven cases in Table 1 are shown and the vertical bar indicates the full range of found values. In the case of the Canadian smoke values (measurement case from 22 Augsut 2017), vertical bars show the retrieval uncertainty.
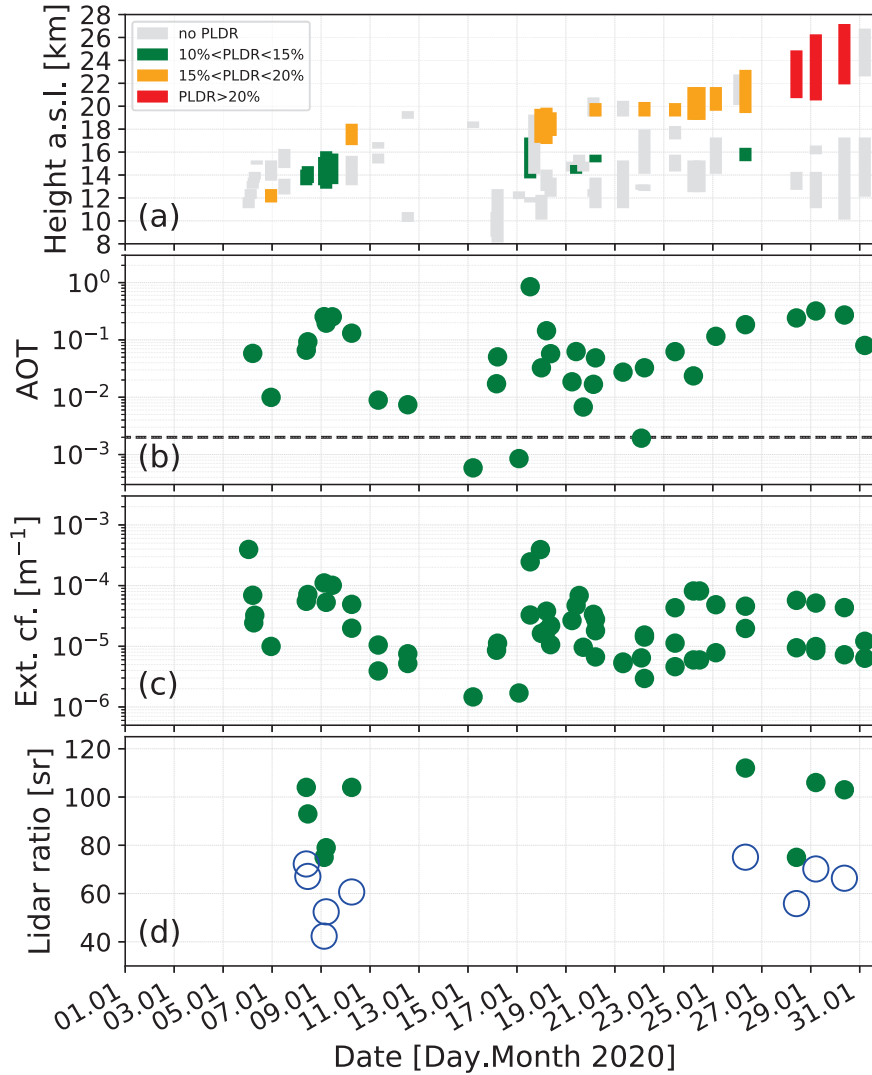
Figure 5. (a) Overview of Polly observations of stratospheric smoke layers (thick bars) from 6-31 January 2020. The color of the bar indicates the layer mean 532 nm particle linear depolarization ratio (PLDR). If no trustworthy PLDR solution could be obtained, the bars are grey. (b) 532 nm AOT of the stratospheric smoke, calculated from the profiles of the smoke backscatter coefficients multiplied by a lidar ratio of 95 sr, (c) layer mean 532 nm particle extinction coefficient, and (d) layer mean 532 nm lidar ratio (green) obtained from the nighttime Raman lidar measurements. The open blue circles indicate estimated 355 nm lidar ratios obtained by means of the combined lidar-photometer retrieval method (see text). The dashed horizontal line in (b) shows background AOT level for the southern hemispheric stratosphere (Sakai et al., 2016). The different smoke transport regimes below and above 19-20 km height as defined in Sect.3.1 are responsible for the two layer structure (in a) observed after 20 January 2020.